Nieto-Sanchez *et al. Molecular Cancer* (2026) 25:21
https://doi.org/10.1186/s12943-025-02542-0

Molecular Cancer

RESEARCH Open Access

Selective genome editing of amplified oncogenes triggers immunogenic cell death and tumor remodeling

A. Nieto-Sanchez[1†], M. Martinez-Lage[1†], P. Puig-Serra[1], S. Carpintero[1], A. Alonso-Yanez[1], P. Ojeda-Walczuk[2,3,4], M. Ibañez-Navarro[5], G. Pita[6], FJ. Moya[1], C. Moreno[1], MC. Martin[1], R. Alonso[6], R. Nuñez-Torres[6], VJ. Sanchez-Arevalo Lobo[7,8], L. Alonso-Guirado[9], N. Malats[9], A. Gonzalez-Neira[4,6], L. Fernandez[5], P. Roda-Navarro[10], R. Torres-Ruiz[1,2,3,4*] and S. Rodriguez-Perales[1*]

Abstract

Oncogene amplifications fuel some of the most lethal, therapy-refractory cancers, yet remain clinically untargeted. We report a single-guide CRISPR/Cas9 strategy that converts the sheer copy-number excess of oncogene amplicons into an Achilles' heel. A solitary intronic double-strand break is innocuous in diploid genomes but collapses oncogene amplification-positive cells across neuroblastoma, small-cell lung and colorectal carcinoma models, driving > 90% loss of viability, G_2/M blockade and catastrophic DNA-damage signalling. Amplified-locus cleavage rewires transcription toward cell death activation, necroptosis and cGAS–STING–mediated immunogenic cell death, enabling dendritic-cell cross-priming and T-cell activation and proliferation. In xenografts, delivery of the intronic sgRNA shrinks tumours by 90%, prolongs survival and remodels the innate tumour microenvironment. Deep sequencing confirms negligible off-target editing, and combination with doxorubicin achieves supra-additive killing. These findings establish amplification density, not sequence content, as a tractable, tumour-exclusive target and unveil a dual-action platform that is simultaneously cytotoxic and immunostimulatory. Editing of tumor amplifications therefore offers a blueprint for translating copy-number aberrations into precision genome-editing therapies for treatment-resistant cancers.

Keywords Cancer targeted therapy, Genome editing, Oncogene amplification, ecDNA, Immunogenic Cell Death (ICD), CRISPR system, Preclinical studies

†A. Nieto-Sanchez and M. Martinez-Lage contributed equally to this work.

*Correspondence:
R. Torres-Ruiz
rtorresr@cnio.es
S. Rodriguez-Perales
srodriguezp@cnio.es

Full list of author information is available at the end of the article

Main

Oncogene amplification (OA) is among the most pervasive genetic mechanisms that drive malignant progression, therapeutic resistance and poor prognosis [1–4]. Pan-cancer sequencing analyses now estimate that about one-third of all cancer patients present tumours whose growth is driven by OA [5]. Amplified oncogenes occur in two principal, non-mutually-exclusive architectural states: (i) circular extrachromosomal DNA (ecDNA) that replicates and segregates independently of chromosomes, and (ii) homogeneously staining regions (HSRs) embedded within chromosomal arms [6–8]. Both configurations elevate oncogene dosage, yet ecDNAs typically achieve the highest copy numbers and transcriptional output [6, 9, 10]. The two architectures are dynamically interconnected: ecDNA can reintegrate into chromosomes to seed new HSR amplicons, whereas bridge-fusion-break (BFB) cycles and chromothripsis can excise chromosomal fragments to regenerate ecDNA [6, 11]. Repeated cycling between extrachromosomal and intrachromosomal states generates extreme copy numbers, fuels intratumoral heterogeneity and accelerates tumor evolution [8, 12, 13]. The clinical consequences of OA are profound.

This dynamic capacity allows ecDNA-driven cancers to quickly escape current therapies [14]. As a result, the presence of high-copy OAs (especially on ecDNA) correlates with treatment-refractory disease and poor outcomes. Indeed, amplification of *MYC* or *MYCN*, for example, define aggressive variants of colorectal adenocarcinoma, small-cell lung cancer (SCLC) and neuroblastoma (NB) that frequently evade current therapies [15–21]. These tumors also tend to be immunologically "cold": *MYC* overexpression is strongly correlated with suppression of inflammatory gene programmes and paucity of tumor-infiltrating lymphocytes [22, 23]. Thus, OA confers both intrinsic therapy resistance and extrinsic immune evasion.

Despite its importance, there is no approved therapy that selectively eliminates amplification-positive cancer cells [24]. Conventional treatments (e.g. chemotherapy, kinase inhibitors) often fail to durably control tumors with amplified oncogenes, as these lesions enable tumors to rapidly adapt or develop drug resistance [14, 24]. Recent studies suggest that the amplified DNA itself is a quantifiable vulnerability: CRISPR nucleases can induce lethal numbers of double-strand breaks (DSBs) when directed to high-copy loci, while sparing normal cells with only two alleles [25–27].

Here, we introduce a single sgRNA CRISPR/Cas9 approach that leverages intronic targeting within amplified oncogenic loci. A solitary intronic double strand break (DSB) is well-tolerated in diploid genomes but would fragment the genome of tumor cells carrying dozen of DSBs across their amplified oncogene loci, triggering irreparable damage and cell death. Beyond direct cytotoxicity, the massive locus-specific damage activates the cGAS–STING innate immune sensing pathway [28, 29], and precipitates immunogenic cell death (ICD), converting an otherwise immune-silent tumour into an immune cell infiltrated tumour. In xenograft models, adenoviral delivery of the intronic sgRNA collapses *MYCN* amplicons, remodels the tumour micro-environment and induces durable tumour growth control. These data establish OA density as a tractable, tumour-specific liability and provide a dual-action framework, cytotoxic and immunostimulatory, for treating refractory amplification-driven cancers.

Results

Selective cytotoxicity in high-copy number amplified tumour cells across lineages

Copy number (CN) status has been linked to the magnitude of CRISPR-induced depletion. Analysis of uncorrected DepMap data (pre-Chronos) across the cancer cell-line compendium revealed a progressive increase in gene effect strength with rising absolute CN, followed by a plateau at very high levels (> 40–50 copies) (Fig. 1a). To exploit this genomic vulnerability, we engineered single sgRNAs that cleave unique, non-coding intronic sequences within the amplified loci of *MYC* (intron 2), *MYCN* (intron 1), *EGFR* (intron 22), *CDK4* (intron 7) and *ERBB2* (intron 7) (Fig. 1b). Target sites were selected to avoid CpG islands, promoter regions and annotated regulatory chromatin, thereby minimizing off-target activity and preserving gene function in non-amplified cells (Supplementary Fig. 1a-e). Delivery of a single intronic sgRNA targeting *MYC*, *MYCN*, *EGFR*, *CDK4* or *ERBB2* was sufficient to elicit profound cytotoxicity in six independent amplification-positive models: KELLY^{A} (NB, *MYCN*), H69AR^{A} (SCLC, *MYCN*), COLO320^{A} (colorectal cancer, *MYC*), A431^{A} (epidermoid carcinoma, *EGFR*), RH-30^{A} (alveolar rhabdomyodarcoma, *CDK4*) and BT-474^{A} (breast cancer, *ERBB2*), whose focal amplifications were confirmed by FISH (Supplementary Fig. 1f, g). Compared with the safe-harbour control (sgAAVS1), viable-cell counts fell by > 90% within one week (KELLY^{A}, 98.8%; H69AR^{A}, 94.7%; COLO320^{A}, 92.8%; A431^{A}, 97.3%; RH-30^{A}, 94.0%; BT-474^{A}, 99.5%)(Fig. 1c; Supplementary Fig. 2a), and clonogenic growth decreased by 67–99% (KELLY^{A}, 98.6%, H69AR^{A}, 99.1%, COLO320^{A}, 67.4%) (Fig. 1d-e). Cell-cycle profiling showed a concordant two– to three-fold accumulation in G_2/M, indicative of mitotic blockade (Fig. 1f, g; Supplementary Fig. 2b, c). Together, these cell lines span a continuum of copy-number contexts, from high (~ 50 copies; e.g. BT-474^{A}) to very high (> 400 copies; COLO320^{A}) amplification (Supplementary Fig. 1f, g). Across this spectrum,

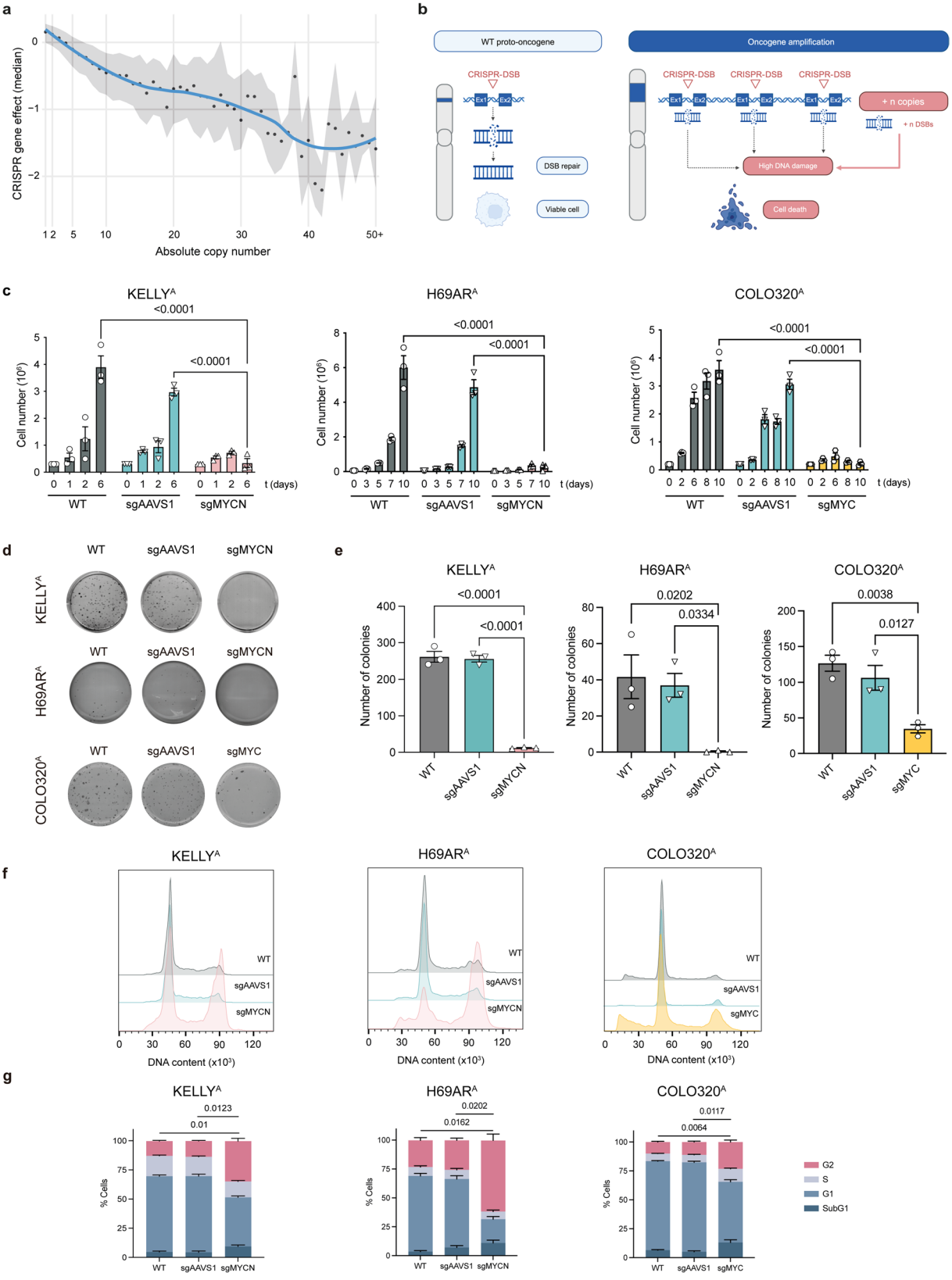

Fig. 1 (See legend on next page.)

(See figure on previous page.)

Fig. 1 Intronic CRISPR cleavage of *MYC*-family amplicons selectively impairs cell viability. **a** DepMap analysis showing the median uncorrected CRISPR gene-effect (pre-Chronos) across all cancer cell lines plotted against the absolute copy number of each corresponding gene. **b** Schematic of the single-sgRNA strategy targeting intronic, non-coding DNA within high-copy amplicons. **c** Cell-proliferation curves for KELLY^{A}, H69AR^{A} and COLO320^{A} following LV delivery of sgMYCN (KELLY^{A}, H69AR^{A}) or sgMYC (COLO320^{A}) versus controls (WT, sgAAVS1) ($n = 3$). **d** Representative colony-formation assays for the same cell lines ($n = 3$; assayed at days 14–21). **e** Quantification of colonies from (d). **f** Cell cycle distributions after intronic targeting (KELLY^{A} and H69AR^{A} at 48 h; COLO320^{A} at 5 days). **g** Quantification of G_2/M enrichment from f. Data are mean ± s.e.m.; one-way ANOVA. Illustration created with BioRender (b). (^{A}) denotes amplification-positive cells

CRISPR-mediated cleavage of the amplified locus (sgMYCN, sgMYC, sgEGFR, sgERBB2, sgCDK4) consistently and strongly suppressed proliferation relative to wild-type and neutral controls (sgAAVS1).

Amplification dependency across NB models

Parallel experiments in an expanded NB panel confirmed that growth inhibition is strictly dependent on *MYCN* amplification status. *MYCN*-amplified IMR-32^{A} and LAN-5^{A} cells, whose amplicon (^{A}) architecture (HSR or ecDNA) was verified by FISH (Supplementary Fig. 1f), were profoundly inhibited (IMR-32^{A}, 98.8%; LAN-5^{A}, 96.6%), whereas non-amplified (^{NA}) SK-N-AS^{NA} and SK-N-FI^{NA} cells were unaffected (Fig. 2a; supplementary Fig. 3a). Colony-formation assays mirrored these findings, showing a marked loss of clonogenicity in amplified cells (IMR-32^{A}, 98.6%; LAN5^{A}, 97.6%) (Fig. 2b, c; supplementary Fig. 3b,c). All amplified models revealed concordant G_2/M arrest (Fig. 2d, e; supplementary Fig. 3e-h). To further dissociate CN–driven toxicity from disruption of the *MYCN* transcription unit, we designed *MYCN*-flanking sgRNAs that induce DSBs within the 2p24 NB amplicon but are positioned outside *MYCN* coding and regulatory regions. These sgRNAs likewise suppressed growth selectively in *MYCN*-amplified cells (sgMYCNflank-1, 91.6%; sgMYCNflank-2, 94.2%) relative to the safe-harbour control (sgAAVS1), while sparing non-amplified controls (Supplementary Fig. 3d).

Biosafety in primary human mesenchymal cells and NB models

To assess biosafety in both normal and tumour contexts, we performed proliferation and genome-wide off-target analyses in telomerase inmortalized human mesenchymal stem cells (hMSC-TERT), alongside targeted off-target validation in NB cell lines. In hMSC-TERT, proliferation assays, GUIDE-seq, and optical genome mapping (OGM) were used to evaluate tolerability and genomic integrity. Consistent with our design principles (intronic, non-regulatory targeting and CN–dependent toxicity), hMSC-TERT tolerated the intervention without detectable loss of proliferative capacity (Supplementary Fig. 4a). GUIDE-seq and OGM did not reveal recurrent off-target events above predefined thresholds, and OGM identified no therapy-limiting structural variants associated with the *MYCN* sgRNA (Supplementary Fig. 4b, c). In parallel, targeted deep sequencing of the ten highest-scoring predicted off-target sites in NB models showed no significant indels (Supplementary Fig. 4d; Supplementary Table 1).

DNA-damage response activation and G_2/M arrest. Intronic editing triggered a robust DNA-damage response (DDR) that was restricted to amplification-positive cells. γH2AX foci co-localised with *MYCN* amplicons and were accompanied by DNA-PKcs Ser2056 phosphorylation (Fig. 3a, b; supplementary Fig. 5a, b). Alkaline comet assays confirmed extensive fragmentation (Fig. 3c, d; supplementary Fig. 5c, d), and phosphorylated STING (p-STING) accumulated exclusively in *MYCN*-amplified cells (Fig. 3e; supplementary Fig. 5e), consistent with cGAS-STING activation. Combining intronic CRISPR with doxorubicin (DOX), a first-line DNA-damaging agent for NB, produced supra-additive cytotoxicity in *MYCN*-amplified cells (93–98% additional inhibition versus DOX alone), whereas non-amplified lines or controls derived no additional benefit (Fig. 3f).

Transcriptomic rewiring towards cell death and inflammation

RNA-seq performed 48 h after transduction identified 514 differentially expressed genes (DEGs) (adjusted p-value < 0.05). Hierarchical clustering cleanly segregated sgMYCN-treated samples from controls (Fig. 4a, b). Gene-set enrichment analysis (GSEA) highlighted activation of p53 signaling, necroptosis, TNF–NF-κB and type-I-interferon pathways (Fig. 4c, d), consistent with the DNA-damage and inflammatory phenotypes observed at the protein level (Supplementary Fig. 6a). To determine whether these transcriptional responses were conserved beyond NB, we extended the analysis to the MYCN-amplified SCLC line H69AR, selected for its distinct lineage, genomic arquitecture, and robust MYCN CN. Comparable transcriptomic changes were detected in the *MYCN*-amplified SCLC line H69AR^{A}, confirming the reproducibility of these responses across independent *MYCN*-driven contexts (Supplementary Fig. 6b-e). Because our intronic targeting strategy does not disrupt *MYCN* coding or regulatory sequences, the observed expression shifts likely reflect secondary responses to extensive DNA damage rather than direct transcriptional suppression of *MYCN*.

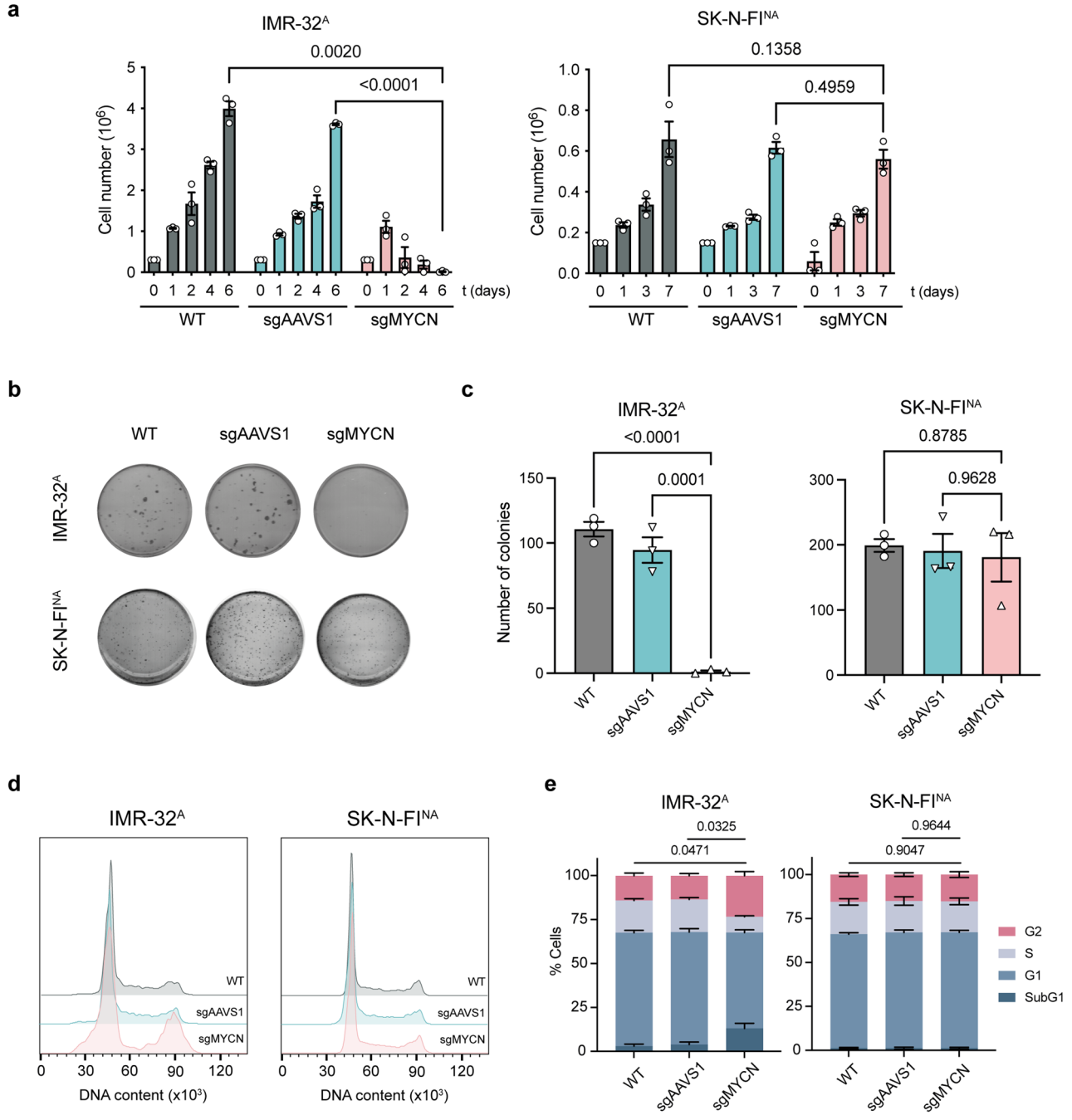

Fig. 2 *MYC*-family intronic editing selectively impairs viability of amplification-positive NB cells. **a** Cell proliferation curves for IMR-32^{A} and SK-N-FI^{NA} cells following LV delivery of sgMYCN or control constructs ($n=3$). **b** Representative colony-formation assays for IMR-32^{A} and SK-N-FI^{NA} ($n=3$; assayed at days 10–15). **c** Quantification of colonies from (b). **d** Cell cycle profiles 48 h after intronic targeting. **e** Quantification of G_2/M enrichment from (d). Data represnet mean ± s.e.m.; one-way ANOVA. (^{A}) denotes amplification-positive cell lines; (^{NA}), non-amplified counterparts

Immunogenic cell death engages dendritic cells and primes T cells

In vitro editing of *MYCN* triggered a death program with features of necroptosis and ICD. Consistent with frequent CASP8 silencing in *MYCN*-amplified tumours, caspase-8 was undetectable, while RIPK1, RIPK3 and phospho-MLKL increased alongside p53/p21 induction and caspase-3 cleavage, indicating a shift toward necroptosis superimposed on DNA-damage signaling. In parallel, upregulation of FAS and BAX suggests extrinsic (FAS-mediated) and intrinsic (BAX-mediated) apoptotic inputs that reinforce a multifaceted ICD response (Fig. 5a; supplementary Fig. 7a, b). All three canonical hallmarks of ICD, surface calreticulin, extracellular ATP

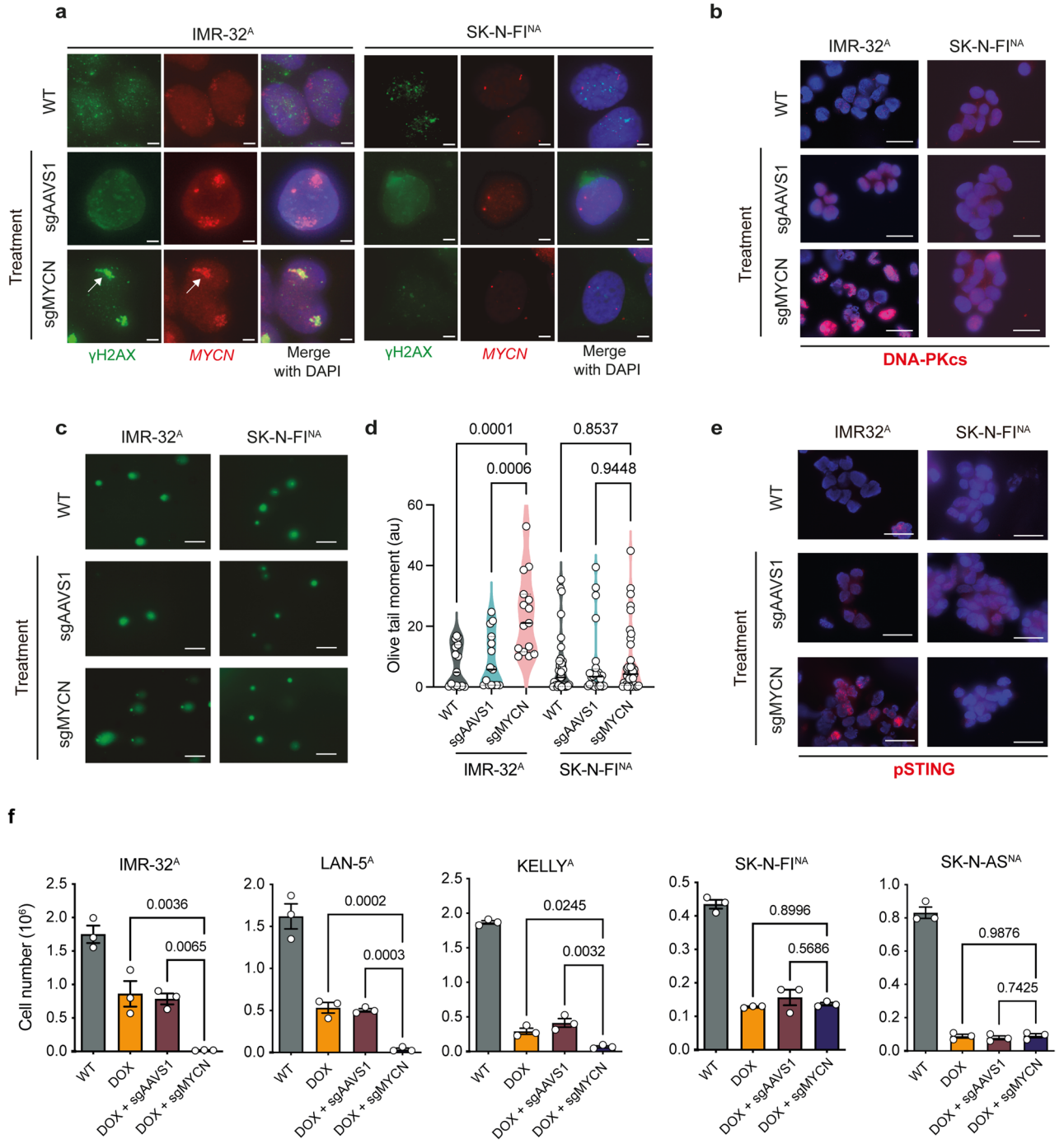

Fig. 3 Intronic sgMYCN induces locus-specific DNA damage response and potentiates doxorubicin response. **a** Immuno-FISH analysis of γH2AX foci (green) and *MYCN* FISH signals (red) in IMR-32^{A} and SK-N-FI^{NA} cells (assayed at 36–48 h). Arrows indicate representative colocalization events. Scale bar, 5 µm. **b** Immunofluorescence staining of phosphorylated DNA-PKcs (Ser2056, red). Scale bar, 50 µm. **c** Representative images from alkaline comet assays showing DNA fragmentation following sgMYCN treatment. Scale bar, 200 µm. **d** Quantification of DNA damage (Olive moment) from (c). **e** Immunofluorescence analysis of phosphorylated STING (red) in IMR-32^{A} and SK-N-FI^{NA} cells. Scale bar, 50 µm. **f** Cell proliferation assays in IMR-32^{A}, LAN-5^{A}, SK-N-FI^{NA}, and SK-N-AS^{NA} cells treated with DOX, DOX + sgAAVS1, or DOX + sgMYCN ($n = 3$ independent experiments). Data are mean ± s.e.m. one-way ANOVA. (^{A}) denotes amplification-positive cell lines; (^{NA}) non-amplified counterparts

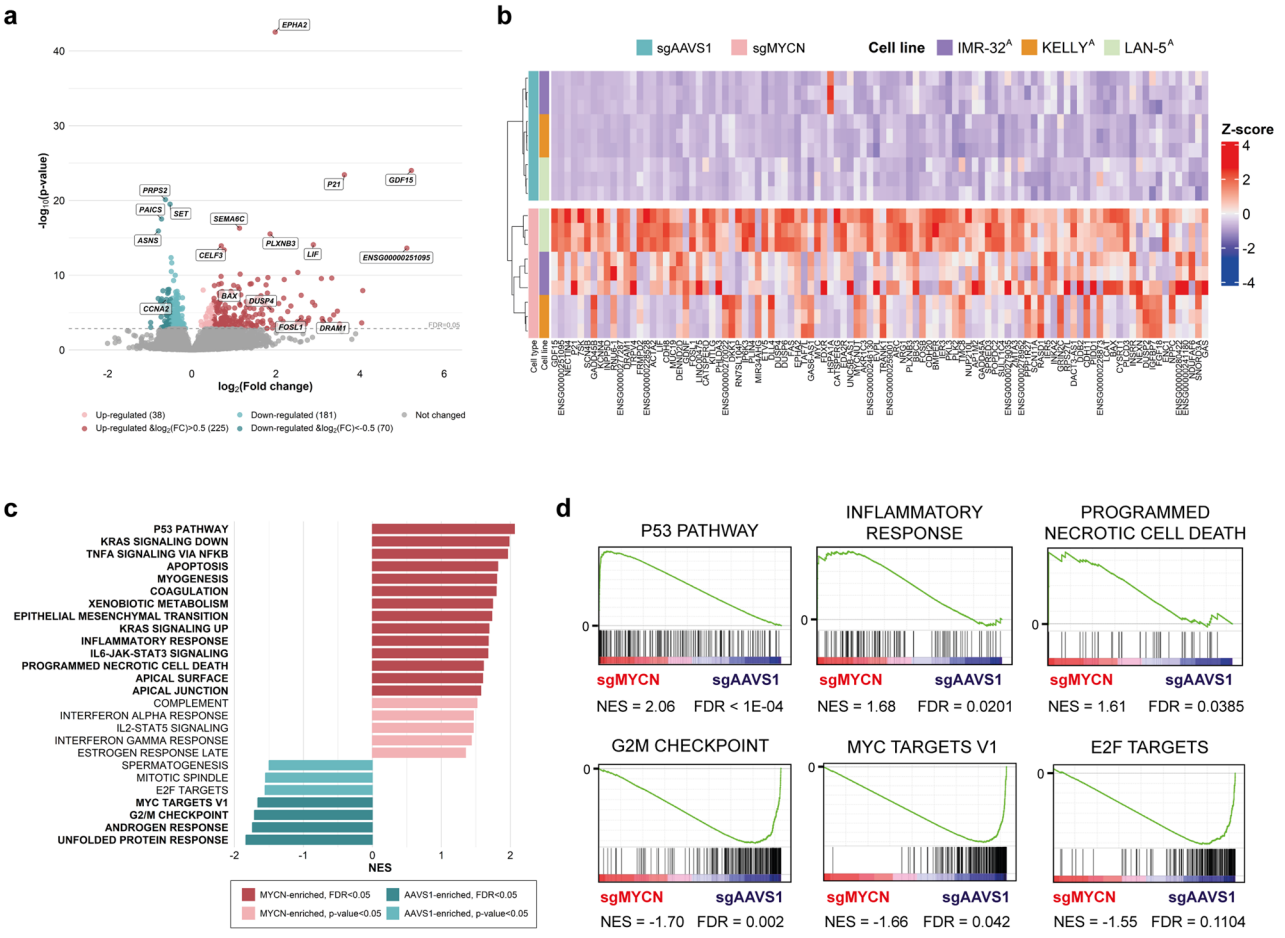

Fig. 4 Transcriptomic profiling of *MYCN*-targeted NB cells reveals activation of cell death and inflammatory pathways. **a** Volcano plot of DEGs between sgMYCN- and sgAAVS1-treated *MYCN*-amplified NB cells ($n = 3$). Red and blue dots indicate significantly upregulated and downregulated genes, respectively; the x-axis shows $\log_2$ fold change and y-axis–$\log_{10}$ adjusted *p*-value. **b** Heatmap showing the top 100 DEGs. **c** GSEA highlighting pathways enriched in sgMYCN-treated cells; normalized enrichment scores (NES) are shown for representative pathways. **d** Network diagram summariaing upregulated and downregulated pathways identified by GSEA. All analyses were performed 48 h post-transduction. (^{A}) denotes amplification-positive cell lines

and HMGB1 release, rose sharply relative to wild-type and sgAAVS1 controls (Fig. 5b; supplementary Fig. 7c-f), providing the danger signals required for innate sensing. Consistently, dying tumor cells were phagocytosed by CD11c^{+} dendritic cells (DC) approximately twice as efficiently as controls, accompanied by DC maturation (Fig. 5c), establising functional engagement of the innate compartment. Functionally, *MYCN*-targeted NB cells enhanced T-cell priming and downstream adaptative responses: CFSE dilution showed robust proliferation with > 2-fold expansion of CD3 + T cells after 9–14 days of co-culture (Fig. 5d, e), accompanied by increased CD25^{+}/CD69^{+} fractions and transcriptional activation of T-cell effector programmes (Fig. 5f, g). Restimulation assays confirmed heightened cytotoxicity against naïve IMR-32^{A} targets (Fig. 5h). Together, these molecular and functional readouts establish in vitro activation of innate and adaptative immunity downstream of intronic CRISPR targeting in *MYCN*-amplified cells. Concordant transcriptomic and ICD readouts in the *MYCN*-amplified H69AR^{A} SCLC model further support reproducibility across oncogene-amplified contexts (Supplementary Fig. 7f, g).

In vivo tumor regression and remodelling of the immune microenvironment

Intratumoral administration of adenoviral AdCas9_sgMYCN into established IMR-32 xenografts yielded a 90% reduction in tumor volume relative to controls (sgMYCN group, 75.24 ± 46.86 mm^3; PBS, 910.83 ± 554.72 mm^3; sgAAVS1, 710.21 ± 265.57 mm^3) (Fig. 6a, b). Extended survival was demonstrated, with 75% of mice surviving beyond day 70, whereas all controls succumbed by day 40 (Fig. 6c). Histology demonstrated widespread apoptosis (cleaved caspase-3) and diminished proliferation (Ki-67) (Fig. 6d, e). Despite the T-cell-deficient background of nude mice, in vivo CRISPR editing provoked a marked influx of CD45^{+}

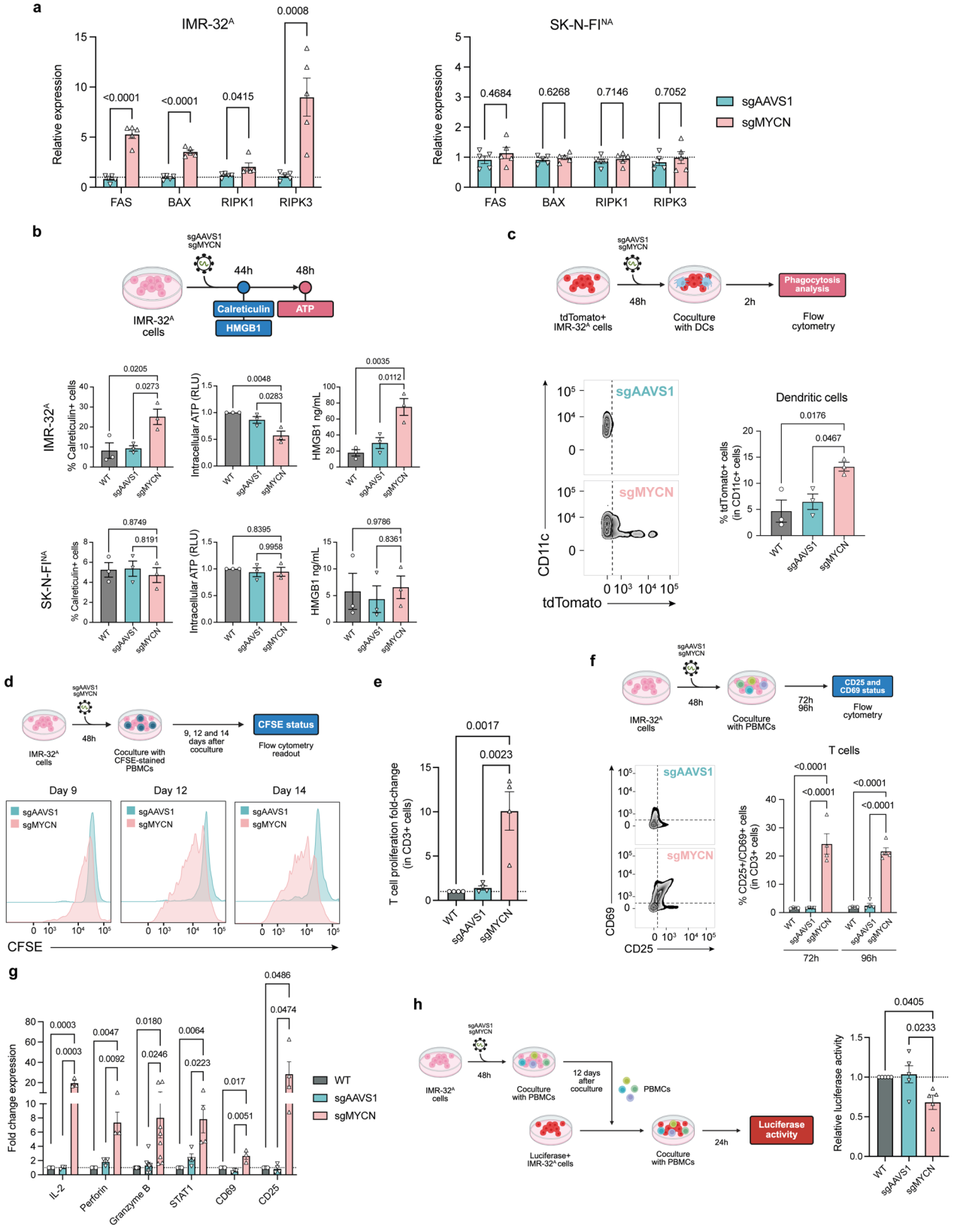

Fig. 5 (See legend on next page.)

(See figure on previous page.)

Fig. 5 Targeting *MYCN* induces necroptosis and hallmarks of immunogenic cell death in NB cells. **a** RT-qPCR of death-pathways genes (*FAS*, *BAX*, *RIPK1*, *RIPK3*) in IMR-32^{A} and SK-N-FI^{NA} cells after sgMYCN or control treatment ($n \geq 3$; assayed at 48 h). **b** ICD marker analysis: workflow (top). Quantification of surface calreticulin exposure, extracellular ATP release and HMGB1 secretion in IMR-32^{A} and SK-N-FI^{NA} cells ($n = 3$; assayed at 44–48 h). **c** DC phagocytosis assay: workflo (top), representative flow plot (left), and quantification of CD11c^{+}/tdTomato^{+} DC (right). **d** T-cell proliferation assay: workflow (top) and representative CFSE profiles of CD3 + cells at days 9, 12 and 14 after co-culture with IMR-32^{A} (WT), sgAAVS1, or sgMYCN cells. **e** Quantification of proliferating CD3 + cells at day 12 from (d) ($n = 4$). **f** T-cell activation assay: workflow (top), representative flow cytometry plots (left) and quantification of CD25^{+}/CD69^{+} cells within the CD3^{+} population at 72 and 96 h of co-culture (right). **g** qRT-PCR of activation-associated transcript in CD4+, CD8 + and shared T-cell populations after 12 days of co-culture ($n \geq 3$). **h** Restimulation (cytotoxicity) assay: workflow (left) and relative growth of luciferase-labelled IMR-32^{A} targets after 24 h co-culture with pre-primed PBMCs (right, $n = 5$). Data are mean ± s.e.m.; one-way Anova. Illustrations created with BioRender (b-d, f, h). (^{A}) denotes amplification-positive cell lines; (^{NA}), non-amplified counterparts

leukocytes, enrichment of F4/80^{+}/CD86^{+} M1-like macrophages and activated DCs, with no expansion of CD163^{+} M2 macrophages (Fig. 6f, g). Immune deconvolution of tumor RNA-seq corroborated these findings, showing enrichment of monocytes and macrophage populations (Supplementary Fig. 8a, b), underscoring the potency of the ICD programme in reprogramming the tumour microenvironment.

Discussion

Selective eradication of cancer cells without collateral damage to normal tissue remains a central and largely unmet goal of precision oncology. Existing genotype-directed strategies, whether they exploit metabolism rewiring [30], endogenous replication stress [31], or DNA-repair defects [32], typically open only narrow therapeutic windows because tumour and host share most biochemical circuitry. In contrast, somatic OAs create a categorical, tumour-exclusive distinction: malignant cells harbour tens to hundreds of additional DNA copies that are virtually absent from healthy tissue. In this context, CRISPR/Cas9 gene editing has emerged as a powerful modality for disrupting oncogenic alterations with high precision. Prior studies have demonstrated the feasibility of targeting tumour-specific mutations [26] and structural rearrangements [33, 34] using CRISPR, paving the way for genetically informed therapeutic interventions. Here we demonstrate that a single intronic sgRNA directed against OAs converts this quantitative abnormality into a potent, dual-action therapeutic modality, simultaneously causing catastrophic DNA damage and triggering ICD [35–38]. The convergence of DDR, necroptosis, and immunogenic signalling suggests that high-copy OA not only confers vulnerability to CRISPR cutting but also rewires tumour–immune crosstalk in a therapeutically actionable way.

OAs are among the most frequent structural aberrations in solid tumours and are virtually absent in normal tissues, making them ideal therapeutic targets [5, 39]. By positioning the CRISPR cut site in non-coding intronic DNA, we decouple cytotoxicity from gene knockout. Non-amplified cells experience just one or two DSBs that are readily repaired, whereas OA-positive cells suffer a lethal burden of breaks that overwhelms repair pathways and activates cell-cycle checkpoints. The concept generalises across architectural states, HSR regions and circular ecDNA, and across multiple lineage-diverse models, underscoring broad translational potential. Importantly, the same design principles proved applicable to multiple oncogenes (*MYC*, *MYCN*, *EGFR*, *ERBB2* and *CDK4*) across six independent amplification-positive models, suggesting that the approach is not restricted to a single locus or tumour type but instead exploits a generic property of high-copy focal amplification.

Across lineage-diverse models, intronic CRISPR targeting of OAs induces near-complete growth arrest, G_2/M blockade and loss of clonogenicity, with negligible impact on non-amplified cancer cells and near-diploid hMSC-TERT controls. Genomes with focal high-copy amplification (tens to hundreds of copies) show marked depletion, whereas aneuploid/polyploid cancer cells lacking OAs do not, delineating the boundary between true amplification-driven vulnerability and mere aneuploidy and supporting a cut-site–number mechanism in which amplification density, rather than gene knockout per se, dictates cytotoxicity.

Expanded analyses in *MYCN*-driven NB models further reinforce this view: *MYCN*-amplified lines with either HSR or ecDNA architecture are consistently sensitive, non-amplified counterparts are spared, and sgRNAs positioned in *MYCN*-flanking regions outside coding and regulatory elements reproduce the same amplification-dependent phenotype. Thus, both intronic and flanking designs converge on a model in which local DSB burden within the amplicon, rather than transcriptional silencing of the driver gene, is the dominant determinant of response. The breadth of this effect underscores the generalizability of the platform for OA-related malignancies, which are characterised by high genomic instability (in NB, SCLC and colorectal CIN subtype carcinoma) and immune exclusion, settings in which this strategy may be particularly impactful. Importantly, supra-additive killing with doxorubicin indicates that locus-specific CRISPR damage can be layered onto existing genotoxins to widen the therapeutic index [40]. Focal high-level amplification of oncogenes such as *MYC*, *EGFR*, *ERBB2*, and *CDK4*, which generate tens to hundreds of gene copies per cell, therefore represent clinically relevant contexts

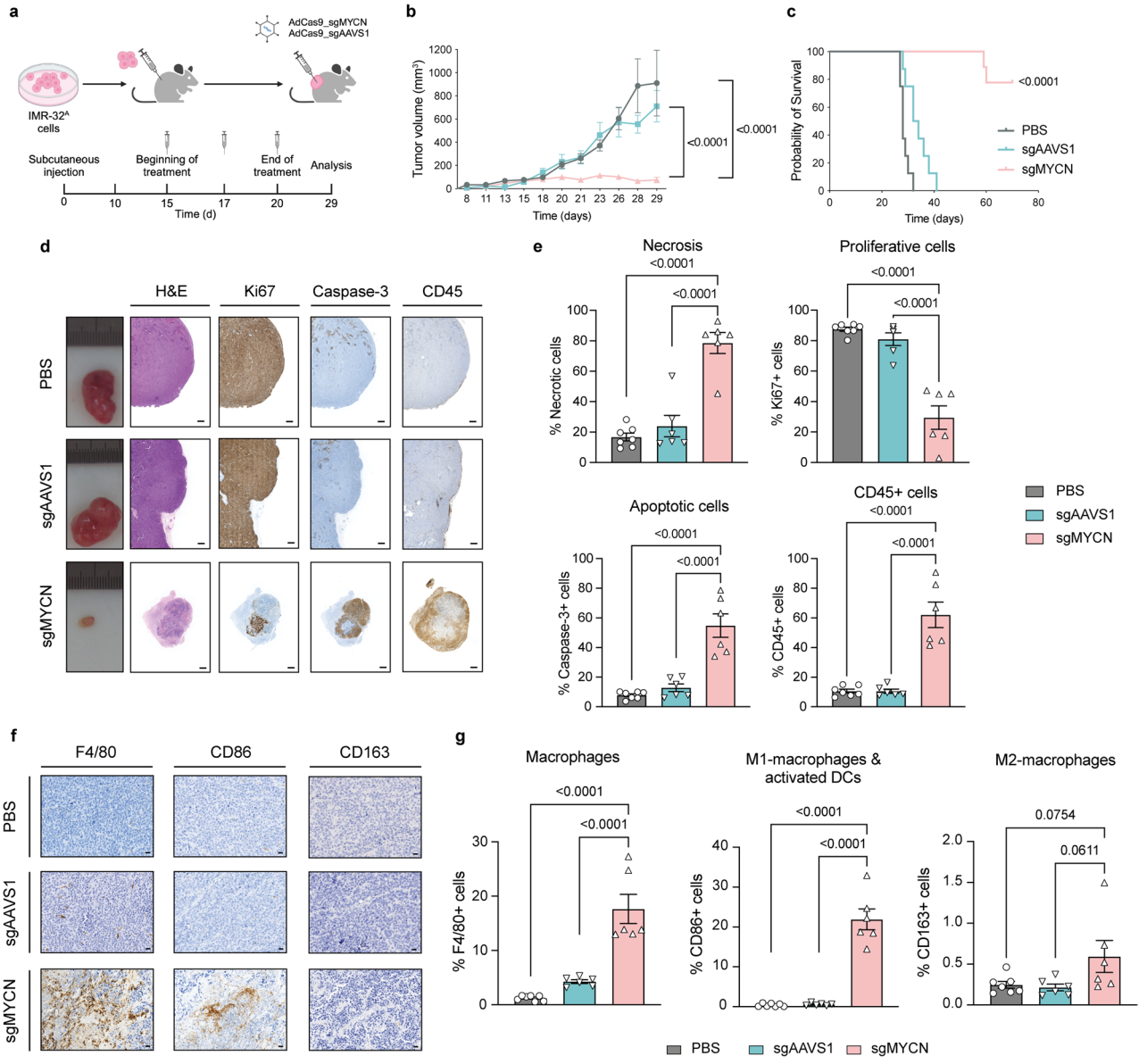

Fig. 6 In vivo CRISPR targeting of *MYCN* suppresses tumor growth and remodels innate immune. **a** Schematic of intratumoral AdV delivery in IMR-32 A xenografts. **b** Tumor-growth kinetics (PBS, sgAAVS1 or sgMYCN; $n = 12$). **c** Kaplan–Meier survival analysis. **d** Representative H&E, Ki67, cleaved caspase-3 and CD45 staining. Scale bar, 500 µm. **e** Quantification of histological markers shown in d. **f** Immunohistochemistry of tumor sections showing F4/80⁺, CD86⁺ and CD163⁺. Scale bar, 20 µm. **g** Quantification of immune cell populations depicted in f. Data are mean ± s.e.m.; two-way ANOVA (tumour volume), log-rank test (survival), one-way ANOVA (histological and IHC). Illustration created with BioRender (a)

for this strategy. Genome-wide off-target analyses in primary hMSCs-TERT cells further support the safety of this approach: proliferation remained intact and neither GUIDE-seq nor OGM detected therapy-limiting structural variants or recurrent off-target edits. Taken together with the the dependence of CRISPR toxicity on local copy number, these findings point to a wide therapeutic window separating tumour from normal tissue.

In NB cells, amplified-locus cleavage initiates a predictable sequence of events: massive DSB accumulation, G_2/M arrest, necroptosis and release of danger-associated molecular patterns (calreticulin, HMGB1, ATP). These biochemical changes are consistent with established features of ICD and suggest that *MYCN*-driven tumours may become more permissive to antitumour immune activation, although, definitive vaccine-like effects will require dedicated in-vivo validation. DCs efficiently phagocytosed CRISPR-killed debris and matured, cross-priming naïve T cells that subsequently proliferated, upregulated activation markers and exerted cytotoxic activity against *MYCN*-expressing targets. Transcriptomic profiling complements these observations: intronic

editing activates p53 signalling, necroptosis, TNF–NF-κB and type-I interferon pathways, providing a mechanistic bridge between locus-specific DNA damage and inflammatory cell death. Thus, even in the absence of in vivo models with intact adaptive immunity, these data support functional engagement of the innate and adaptive immune arms. Notably, concordant transcriptional and ICD signatures in the SCLC model indicate that this immunogenic programme is reproducible across independent contexts.

Intratumoural adenoviral delivery of sgMYCN curtailed xenograft growth by > 90%, extended survival and remodelled the tumour microenvironment despite the T-cell deficiency of nude mice. The marked influx of F4/80^{+}/CD86^{+} macrophages and activated dendritic cells, coupled with the absence of CD163^{+} M2 macrophages [23, 41–43], highlights a shift toward an inflammatory milieu. Given that ecDNA-rich tumours are frequently refractory to checkpoint blockade, such innate activation may constitute a prerequisite for subsequent adaptive engagement. Future in-vivo studies in immunocompetent and humanised models will be required to define the durability, antigen specificity and systemic reach of these responses.

Three features make this platform attractive for clinical translation: (i) genetic specificity, dictated by amplicon copy number; (ii) mechanistic versatility, combining lethal DNA damage with ICD; and (iii) architectural agnosticism, working in both HSR and ecDNA contexts. The latter is critical, as ecDNA-encoded oncogenes drive extreme heterogeneity and drug resistance [13, 24]. CRISPR fragmentation of ecDNA could therefore thwart rapid evolutionary escape routes unavailable to chromosome-bound loci. Future studies should test sgRNA efficacy in models of adaptive resistance driven by ecDNA re-expansion [10, 12], and in patient-derived organoids bearing complex amplicon topologies. Remaining challenges centre on delivery and safety. Finally, high-level focal amplifications are common across multiple oncogenes and cancer types, for example *ERBB2* in breast cancer, *EGFR* in glioblastoma and squamous carcinomas, and *CDK4* in sarcomas. These prevalence patterns delineate clinically relevant settings in which a copy-number–driven CRISPR strategy may have clinical impact.

Systemic deployment will benefit from emerging technologies, including high-fidelity Cas9 variants [44], chemistry-stabilised sgRNAs [45], liver-de-tropised lipid nanoparticles [46], and programmable virus-like particles [47], that collectively enhance tissue selectivity and minimise off-target editing. Synergistic pairing with DNA-damaging chemotherapy or immune-checkpoint inhibitors offers rational combination avenues to tackle historically undruggable, immune-silent MYC tumours [48, 49], as suggested by the supra-additive effects observed with doxorubicin in *MYCN*-amplified models.

In summary, we re-cast OA density as an intrinsic liability that can be therapeutically exploited by precision genome editing. By weaponising the very driver of therapeutic resistance, intronic sgRNA CRISPR editing delivers a two-pronged assault, cytotoxic and immunogenic, that extends across multiple oncogenes, copy-number architectures and tumour lineages. Although further work on delivery, long-term safety and immune integration is required, our findings position copy-number–driven CRISPR targeting as a promising framework for the treatment of amplification-driven malignancies.

Methods

DepMap copy-number analysis

CRISPR gene-effect scores without Chronos correction (pre-Chronos) and gene-level absolute copy number were retrieved from the DepMap portal (https://depmap.org/portal/). For each gene, we paired the uncorrected gene-effect values across all DepMap cell lines with the corresponding absolute copy numbers and computed the median gene effect per copy-number. The resulting medians were visualized against absolute copy number using LOESS smoothing (span = 0.5) with 95% confidence intervals obtained by bootstrap resampling (1,000 iterations). Analyses were performed in R (v4.3) with base stats and ggplot2.

Cell culture

IMR-32^{A}, SK-N-FI^{NA}, SK-N-AS^{NA}, HEK293T/17, H69AR^{A}, COLO320^{A}, A431^{A} and BT-474^{A} cell lines were obtained from the American Type Culture Collection (ATCC: CCL-127, CRL-2142, CRL-2137, CRL-1573, CRL-11351, CCL-220, CRL-1555 and HTB-20, respectively). The LAN-5^{A}, KELLY^{A} and RH-30^{A} cells were sourced from the German Collection of Microorganisms and Cell Cultures GmbH (DSMZ: ACC-673, ACC-355 and ACC-489). IMR-32^{A}, LAN-5^{A} and H69AR^{A} cells were cultured in RPMI medium (Gibco) supplemented with 20% fetal bovine serum (FBS, Life Technologies) and 0.1 mM non-essential amino acids (NEAA, Gibco). RH-30^{A} cells were cultured in RPMI medium supplemented with 10% FBS. COLO320^{A} and KELLY^{A} cells were maintained in RPMI with 10% FBS and 10 mM sodium pyruvate. SK-N-FI^{NA} and SK-N-AS^{NA} were cultured in DMEM (Lonza) with 10% FBS and 0.1 mM NEAA (Gibco), while hMSC-TERT [33], HEK293T/17, A431^{A} and BT-474^{A} cells were cultured in DMEM supplemented with 10% FBS. All media included 1% Glutamax (Life Technologies) and 10 mg/ml penicillin-streptomycin (Gibco). Cells were incubated at 37 °C in a humidified incubator with 5% CO2 and 5% O2. Dose-dependent treatments with DOX (S1208, Selleckchem)

were applied: 0.02 µM for IMR-32^{A}, 0.1 µM for LAN-5^{A}, 0.3 µM for KELLY^{A}, 0.5 µM for SK-N-FI^{NA} and 1.75 µM for SK-N-AS^{NA}. tdTomato + IMR-32^{A} cells were generated via transduction with LVs using the pUltra-Chili-Luc transfer plasmid (Addgene #48688), followed by cell sorting. All cell lines were regularly tested to absence of mycoplasma contamination.

sgRNA design and vector construction

sgRNAs were designed using the Benchling CRISPR gRNA Design tool (www.benchling.com) and cloned into the LentiCRISPRv2 vector expressing *Streptococcus pyogenes* Cas9 (spCas9) (Addgene #52961). Cloning involved annealed and phosphorylated oligonucleotides (Sigma-Aldrich) targeting specific sequences, with transformations conducted in Stbl3 bacteria (Thermo Fisher Scientific). Detailed sgRNA sequences are listed in Supplementary Table 2.

Fluorescent in situ hybridization (FISH) and immuno-FISH

Cells were arrested in metaphase using KaryoMAX colcemid (Thermo Fisher Scientific), treated with hypotonic solution (0.075 M KCl, Merck), and fixed with Carnoy's solution (methanol: acetic acid 3:1, Sigma-Aldrich). Following slide spreading, cells underwent dehydration, denaturation and hybridization at 37 °C using an OA FISH probe (Leica Biosystems, Zytovision). Post-hybridization washes were conducted in 20xSSC/Tween-20 buffer at 63 °C. Counterstaining was performed using DAPI in Vectashield mounting medium (Vector Laboratories). For immuno-FISH, cells were pre-incubated with an anti-phospho-histone gH2AX antibody (Ser139) (Clone JBW301, Millipore) prior to MYCN FISH probe hybridization. FISH signals manually were scored by counting nuclei with amplification signals using a Leica DM5500B microscope equipped with a DFC290 color digital camera. Image analysis was performed using Cytovision software v7.4 (Leica Biosystems). Detailed probes and antibody information is provided in Supplementary Table 2.

Lentivirus production, titration and transduction

Recombinant LVs were produced via transient transfection of HEK293T/17 cells, as previously described [50]. Briefly, cells were seeded at 1.1 × 10^{7} cells per 15-cm dish 24 h prior to transfection. Transfection was performed using Lipofectamine 2000 (Thermo Fisher Scientific), with 14.6 µg and 7.9 µg of second-generation packaging plasmids psPAX2 and pMD.2G (Addgene #12260 and #12259, respectively), along with 22.5 µg of the transfer plasmid. Supernatants were collected 48 h post-transfection, clarified by low-speed centrifugation, and filtered through 0.45-µm PVDF filters (Millipore). LV particles were concentrated via ultracentrifugation at 22,000×g for 2 h at 4 °C using a SW32Ti Beckman rotor. The resulting viral pellet was resuspended in 300 µL of sterile saline solution (Braun) and stored at −80 °C. Viral titers, determined by qPCR-based quantification of vector copy number integrations per genome, ranged from 10^{7} to 10^{8} transduction units per milliliter (TU/mL). Target cells were seeded 24 h before transduction and transduced at a multiplicity of infection (MOI) of 25 unless otherwise specified. After 6 h of incubation at 37 °C, the viral medium was replaced with fresh culture medium to ensure optimal transduction efficiency.

Immunofluorescence

Cells were washed, fixed with 4% paraformaldehyde, and permeabilized. Staining was performed by incubating cells overnight with primary antibodies against DNA-PKc and phospho-STING, followed by Alexa Fluor-conjugated secondary antibodies (ThermoFisher Scientific). Cells were counterstained with DAPI and mounted in ProLong DAPI mounting media (ThermoFisher Scientific). Images were acquired using a Leica DM5500B microscope (Leica Microsystems) equipped with two lasers for excitation at 594 nm (red channel, caspase-3 detection) and 405 nm (blue channel, nuclear DAPI staining). Data were collected sequentially at a resolution of 1024 × 1024 pixels and are representative of all experiments analyzed using Cytovision v7.4 software (Leica Biosystems). A detailed list of the antibodies used is provided in Supplementary Table 2.

Comet assay

Comet assays were conducted using the Comet Assay Kit (Abcam) following the manufacturer's instructions. A cell suspension containing 1 × 10^{5} cells was mixed with comet agarose at a 1:10 ratio (v/v) and layered onto microscopic slides. Slides underwent lysis in a solution containing 146 mM NaCl, 30 mM EDTA (pH 7), 10 mM Tris-HCl (pH 7), and 0.1% N-lauroylsarcosine at 4 °C for 30 min. After electrophoresis and staining with Vista Green DNA Dye, slides were visualized using a Leica DM5500B microscope equipped with a DFC290 color digital camera. DNA damage was quantified by analyzing the Olive Moment (OM) with Open Comet software v1.3, using Image J software v1.54 g.

In vitro colony-forming assay

Colony forming assays were performed 24 h post-transduction with the corresponding LVs. For IMR-32^{A}, LAN-5^{A}, KELLY^{A}, SK-N-AS^{NA} and H69AR^{A} cells, 500 cells per well were seeded in six-well plates and cultured for 10–15 days. Colonies were fixed with methanol, stained with a 0.5% crystal violet solution (Sigma-Aldrich), and counted. For SK-N-FI^{NA} and COLO320^{A} cells, 24 h post-transduction, 500 cells were seeded in methylcellulose

medium (MethoCult™, Stem Cell Technologies) in 3.5-cm plates. After three weeks, colonies were stained overnight with a Nitrotetrazolium Blue chloride solution (NBT, Sigma-Aldrich) and counted. Colonies quantification was performed using Image J software v1.54 g (NIH).

Cell cycle distribution analysis

Flow cytometry was used to assess cell cycle distribution based on DNA content in exponentially growing transduced cells. Cells were pelleted by centrifugation 48 h after treatment for every cell line except A431^{A} and COLO320^{A} (analyzed 5 days after treatment), washed with PBS (Sigma-Aldrich), and fixed in ice-cold 70% ethanol (Sigma-Aldrich). Fixed cells were stored at 4 °C for 24 h before analysis. For DNA content quantification, cells were washed twice in phosphate-citrate buffer (Sigma-Aldrich) and stained with a propidium iodide (PI) solution (50 ug/ml in PBS, Sigma-Aldrich) containing 20 µg/mL RNase A (Qiagen) for 30 min. Cellular DNA content was measured on a BD FACSCanto™ platform (BD Biosciences), and data analysis was performed using FlowJo software v10.0.7 (FlowJo). Gating strategies are provided in Supplementary Fig. 9.

Targeted deep sequencing

Customized PCR primers targeting the on-target region and the top 10 predicted off-target sites of sgMYCN were designed and ordered from Integrated DNA Technologies (IDT) with rhAmpSeq index sequences, as detailed in Supplementary Table 2. Off-target sites were predicted using Cas-OFFinder (http://www.rgenome.net/cas-offinder/). Genomic DNA was extracted from relevant cell samples and used for individual amplification of each target locus. The initial PCR amplification was performed using the rhAmpSeq Library Kit (IDT) under the following conditions: 98 °C for 30 s, followed by 23 cycles of 98 °C for 10 s, 60 °C for 30 s, 72 °C for 40 s, and a final extension at 72 °C for 2 min. PCR products were purified using Agencourt AMPure XP beads (Beckman Coulter). A second PCR was performed to attach Illumina-indexed adaptor primers under the following conditions: 95 °C for 3 min, followed by 18 cycles of 95 °C for 15 s, 60 °C for 30 s and 72 °C for 30 s, and a final extension at 72 °C for 1 min. The resulting PCR products were purified using Agencourt AMPure XP beads at a PCR product-to-bead ratio of 1:1. Purified libraries were quantified and sequenced on an Illumina MiSeq sequencing platform using a 300-bp paired-end cycle. Sequencing data were analyzed using CRISPR RGEN Tools Cas-Analyzer software.

RNA sequencing and bioinformatic analysis

Total RNA was extracted from NB cells using the RNeasy Mini Kit (Qiagen). RNA concentration and integrity were assessed using the Qubit RNA HS Assay Kit on a Qubit 3.0 Fluorometer (Thermo Fisher Scientific). Complementary DNA (cDNA) sequencing libraries were generated using the QuantSeq 3' mRNA-Seq V2 Library Prep Kit (FWD, Lexogen), which incorporates reverse transcription with oligo(dT) priming followed by random-primed second-strand synthesis. Unique Molecular Identifiers (UMIs) were included to facilitate molecular tracking and eliminate PCR duplicates during analysis. Libraries were sequenced on an Illumina NovaSeq X platform using NovaSeq X Series Reagent Kits. Base-calling and quality score assignment was performed using Real-Time Analysis software (RTA v2, Illumina). Binary base call (BCL) files were converted to FASTQ format using bcl2fastq2 (Illumina). Sequence reads were trimmed to remove adapter sequences and low-quality bases using Trimmomatic v0.36. Trimmed reads were mapped to the *Homo sapiens* GRCh38 reference genome (ENSEMBL) using STAR aligner v2.5.2b. The resulting BAM files generated were used for downstream analysis.

Mapping and quantification: Unique gene hit counts were calculated using featureCounts from the Subread package v1.5.2, summarizing hits based on the gene_id feature in the annotation file. Strand-specific reads were counted where applicable. Gene counts were processed in R using DESeq2 for differential expression analysis. Significant differentially expressed genes were identified based on an adjusted p-value threshold of <0.05. Gene counts were normalized per DESeq2 protocols to ensure accurate comparisons between conditions.

Deconvolution analysis: Sequencing reads underwent preprocessing to remove adapter sequences and low-quality bases, followed by UMI extraction and PCR duplicate removal to ensure analysis of unique reads. Reads were initially aligned to the human genome using STAR, generating human-specific BAM files. A secondary alignment was performed against the mouse genome. Reads mapping to both genomes were resolved using the Disambiguate tool to ensure species specificity. The resulting human- and mouse-specific BAM files were quantified using HTSeq-count, with read counts converted to transcripts per million (TPM).

Immune deconvolution: The immune cell composition of samples was analyzed using the mMCP-counter tool.

Western blotting

Proteins were extracted using RIPA buffer (50 mM Tris-HCl, pH 8, 150 mM NaCl, 1% Triton X-100, 0.1% sodium deoxycholate, and 0.1% SDS) supplemented with Complete Protease Inhibitor Cocktail Tablets (Roche Applied Science) and PhosSTOP (Roche), as required. Protein separation was performed by SDS-PAGE, followed by transfer onto PVDF membranes (Millipore) using the Trans-Blot Turbo Transfer device

(BioRad). Membranes were blocked and incubated with specific primary antibodies, as detailed in Table S2. HRP-conjugated secondary antibodies were used for detection. Blots were developed using enhanced chemiluminescence (ECL) reagent (GE Healthcare), and signal detection was performed on films (Fujifilm), which were subsequently scanned for analysis using Image J software v1.54 g.

Quantitative reverse transcription-polymerase chain reaction (qRT-PCR)

Total RNA was extracted using the RNeasy Mini Kit (Qiagen) according to the manufacturer's protocol and quantified by spectrophotometry. cDNA synthesis was carried out using the High-Capacity cDNA Reverse Transcription Kit (ThermoFisher Scientific). qRT-PCR was performed in 384-well plates using 2×SYBR Green Master Mix (Thermo Fisher Scientific) on a QuantStudio 6 detection system (Thermo Fisher Scientific). Target gene expression was normalized to the housekeeping genes *GUSB*. Each sample was analyzed in triplicate, with at least three 3 independent experiments per condition. Primers used for qRT-PCR are listed in Supplementary Table 2.

Detection of immunogenic cell death markers

Calreticulin translocation: IMR-32^{A}, KELLY^{A}, SK-N-FI^{NA}, H69AR^{A}, A431^{A}, RH-30^{A} and BT-474^{A} cells (1.25×10^5) were seeded in 12-well plates (Biofil) and transduced with either LVCas9_sgAAVS1 or LVCas9_sgMYCN at a MOI of 15 for IMR-32^{A} and H69AR^{A}, and 20 for KELLY^{A} and SK-N-FI^{NA} cells. After 44 h, cells were harvested, stained with Alexa Fluor 647-conjugated anti-calreticulin antibody (EPR3924, Abcam), and incubated with 40 nM tetramethylrhodamine ethyl ester (TMRE, Sigma). Calreticulin-AF647 + cells were quantified using an LSRFortessa flow cytometer (BD Biosciences). Gating strategies are provided in Supplementary Fig. 9.

HMGB1 release: Supernatants were collected 44 h post-transduction, and HMGB1 release was quantified using the Express ELISA Kit (Tecan), following the manufacturer´s instructions. Absorbance was measured using a VICTOR Nivo photometer (PerkinElmer).

Extracellular ATP detection: IMR-32^{A} or KELLY^{A} cells (2×10^4) were plated in 96-well plates (Costar). Following attachment, cells were transduced with the corresponding LVs constructs at the respective MOIs. After 48 h, extracellular ATP levels were measured using the RealTime-Glo Extracellular ATP Assay (Promega) in combination with digitonin (Promega). Luminescence readings were recorded using the GloMax® Navigator System (Promega).

Phagocytosis assay and T cell activation assay

DCs were derived following the protocol described by Konda et al. [51]. To evaluate the phagocytosis activity of DCs against CRISPR-treated NB cells, dTomato + IMR-32^{A} cells were seeded at a density of 3×10^5 in 12-well plates. Cells were transduced with either LVCas9_sgAAVS1 or LVCas9_sgMYCN at a MOI of 15. After 48 h, transduced dTomato + IMR-32^{A} cells were co-cultured with DCs at a 1:1 ratio for 2 h. Cells were stained with anti-CD11c-APC (Miltenyi Biotec) to selectively identify DCs. Phagocytosis uptake was quantified using an LSRFortessa flow cytometer (BD Biosciences) by measuring the proportion of cells positive for both CD11c-APC and dTomato. IMR-32^{A} or H69AR^{A} cells (1.25×10^5) were seeded in 24-well plates and transduced with LVCas9_sgMYCN or control LVCas9_sgAAVS1 at a multiplicity of infection (MOI) of 20. Forty-eight hours post-transduction, tumor cells were co-cultured with freshly isolated, non-activated human peripheral blood mononuclear cells (PBMCs) at a 1:2 ratio (tumor cell: PBMC). At 72 and 96 h of co-culture, all cells were harvested and stained for surface markers using PECy7-conjugated anti-CD3 (clone UCHT1, BioLegend, 300316), APC-conjugated anti-CD25 (clone M-A251, BioLegend, 302610), and PE-conjugated anti-CD69 (clone FN50, BioLegend, 310910). Flow cytometry was performed on a FACS Canto II system (BD Biosciences), and T cell activation was quantified based on CD25 and CD69 expression within the CD3^{+} population. Proliferation was confirmed through CFSE (423801, BioLegend) staining at 9, 12 and 14 days of co-culture within the CD3 + population. 12 days after co-culture T cells were aspirated and co-cultured with naïve luciferase + IMR-32^{A} for 24 h. Naïve IMR-32^{A} cell viability was inferred from luciferase activity after luciferin incubation (Revvity, 122799) and luminiscence readout. Gating strategies are provided in Supplementary Fig. 9.

Adenovirus production

Adenoviral vectors (AdV) were generated by the Viral Vector Production Unit at Universitat Autonoma de Barcelona (UAB). These vectors were designed to co-express sgRNA under the U6 promoter, along with spCas9 and eGFP separated by a 2 A peptide. Recombinant AdV genomes were constructed via homologous recombination between shuttle plasmids and E1-deleted AdV backbones in *Escherichia coli*. Vectors were subsequently transfected into permissive cells for viral production and purified using dual cesium chloride (CsCl) gradient centrifugation. The final viral titers ranged from $10^{11}$to 10^{12} viral particles per milliliter (vp/mL). Aliquots were stored at −80 °C to preserve stability until further use.

Animal experiments

Animal experiments were conducted in compliance with established animal welfare guidelines and were approved by the Ethics Committees of the Instituto de Salud Carlos III and the Comunidad de Madrid. Eight-week-old female athymic nude mice (Hds: Athymic Nude-Foxn1 nu, Charles River) were housed under controlled conditions at the CNIO animal facility. Tumors were induced by subcutaneous injection of 1×10^6 cells suspended in a 1:1 mixture of Matrigel (BD). Tumor growth was monitored regularly and measured with calipers under blinded conditions. Tumor volume was estimated using the formula: volume (mm^3) = (length [mm]) × (width [mm])$^2 \times 0.52$. When tumors reached approximately 100 mm^3, treatment was initiated with three doses of 2.5×10^9 viral particles (vp) in 100 µL of PBS administered every three days. Mice were humanely euthanized when tumors reached a volume of 1500 mm^3. Tumors were collected and processed for histopathological analysis.

Immunohistochemistry

Tumor tissues were fixed overnight at 4 °C in 4% paraformaldehyde (PFA, Sigma-Aldrich) and embedded in paraffin. Tissue Sect. (3 µm) were deparaffinized, rehydrated, and treated with 3% hydrogen peroxide (Merck) to inhibit endogenous peroxidase activity. Heat-induced antigen retrieval was performed before immunostaining. The antibodies used are listed in Table S2. Immunostained sections were imaged using an Olympus AX70 microscope. Quantification of stained areas was performed using QuPath software v0.5.1, and labeling index (percentage of positively stained cell area) was calculated.

Optical genome mapping

For each cell line, $\sim 1.5 \times 10^6$ cryopreserved cells were used to isolate ultra-high molecular weight (UHMW) gDNA following the manufacturer's instructions (Bionano Prep SP Frozen Cell Pellet DNA Isolation Protocol). DNA quantity was assessed with Qubit™ dsDNA BR assay kit, and 750 ng of UHMW gDNA were labeled using the Direct Label and Stain G2 (DLS-G2) chemistry according to the provider's protocol. Labeled molecules were stored overnight at room temperature, re-quantified, loaded onto Saphyr chips (v3.3), and imaged on the Saphyr instrument to a target yield supporting ~ 300x genome coverage, enabling detection of structural variants (SVs) at ≥ 5% variant allele fraction (VAF). Data processing and variant calling. Molecules were processed with Bionano Solve (v.3.8.2) using the Guided Assembly—Low Allele Frequency pipeline and visualized in Bionano Access v1.8.2. Molecule maps were aligned to GRCh38/hg38, and algorithms were applied to detect insertions, deletions, duplications, inversions, and intra-/interchromosomal translocations, as well as large copy-number alterations (CNAs). Default confidence filters were used for initial SV calls (e.g., insertion = 0; deletion = 0; inversion = 0.02; duplication = 0; intrafusion = 0.02; inter-translocation = 0.02). Events were retained only if (i) absent from the paired control line, (ii) supported by ≥ 3 labels, and (iii) not present in the Bionano control database. CNAs were called at confidence ≥ 0.99 with a minimum size of 500 kb. Additional filters included frequency (< 1% in the internal database), non-masked genomic location, and VAF ≥ 5% supported by ≥ 10 molecules. Paired and locus-focused analyses. For each model, a paired analysis was performed using the Dual Variant Annotation workflow to prioritize variants specific to the edited condition (e.g., sgMYCN) and to annotate events intersecting the 2p24/MYCN locus. Results were reviewed in Access and exported together with quality metrics for downstream integration.

GUIDE-seq

Genome-wide detection of CRISPR/Cas9-induced DSBs was performed by GUIDE-seq as described in detailed by Malinin et al. [52]. Brieftly, cells were electroporated with Cas9-sgRNA ribonucleoprotein (RNP) complexes together with a phosphorothioate-protected double-stranded oligodeoxynucleotide (dsODN) tag that integrates at nuclease-induced DSBs. After ~ 4 days in culture, genomic DNA was extracted and processed for GUIDE-seq "plus" library preparation using anchored, tag-specific PCR; libraries were constructed and sequenced on an Illumina MiSeq using the v3 600-cycle paired-end chemistry. Reads containing dsODN junctions were aligned to GRCh38 and analysed using the open-souce GUIDE-seq pipeline [53] to identify, quantify, and annotate on-target and off-target sites, leveraging the characteristic bidirectional outward-mapping signature at cleavage loci.

Statistical analyses

All statistical analyses were conducted using GraphPad Prism v10.1.1 (GraphPad Software). Data are represented as the mean ± SEM, with the number of independent experiments (n) specified in each figure legend. Data from three or more independent experiments were analyzed using the appropriate statistical test, as indicated in the figure legends. Exact *p* values are reported in the graphs.

Reporting summary

Further information on research design is available in the Nature Research Reporting Summary linked to this article.

Abbreviations

AdCas9_sgMYCN/sgAAVS1	Adenoviral vector expressing Cas9 and a sgRNA targeting MYCN or AAVS1
AdV	Adenovirus vector
ANOVA	Analysis of Variance
ATP	Adenosine triphosphate
BAX	BCL-2-associated X protein
BFB	Bridge-Fusion-Break cycles
cGAS	Cyclic GMP-AMP synthase
Cas9/spCas9	CRISPR-associated nuclease (Streptococcus pyogenes variant)
CFSE	Carboxyfluorescein succinimidyl ester
CRISPR	Clustered Regularly Interspaced Short Palindromic Repeats
DC	Dendritic cell
DDR	DNA-damage response
DEG(s)	Differentially expressed gene(s)
DNA-PKcs	DNA-dependent protein kinase catalytic subunit
DOX	Doxorubicin
DSB/DSBs	Double-strand break(s)
ecDNA	Extrachromosomal DNA
ELISA	Enzyme-Linked Immunosorbent Assay
FAS	Fas receptor (CD95)
FBS	Fetal bovine serum
FISH	Fluorescence in situ hybridization
GAPDH	Glyceraldehyde-3-phosphate dehydrogenase (housekeeping gene)
GFP	Green Fluorescent Protein
GSEA	Gene Set Enrichment Analysis
GUSB	β-Glucuronidase (housekeeping gene)
H&E	Hematoxylin and eosin (histology stain)
HSR/HSRs	Homogeneously staining region(s)
IHC	Immunohistochemistry
ICD	Immunogenic cell death
LV	Lentiviral vector
MLKL	Mixed Lineage Kinase domain-Like pseudokinase
MOI	Multiplicity of Infection
NB	Neuroblastoma
NES	Normalized Enrichment Score
NF-κB	Nuclear Factor kappa-light-chain-enhancer of activated B cells
OA	Oncogene amplification
RIPK1/RIPK3	Receptor-Interacting Protein Kinase 1/3
s.e.m.	Standard error of the mean
sgRNA	Single-guide RNA
SCLC	Small-cell lung cancer
STING/p-STING	Stimulator of Interferon Genes (total or phosphorylated)
TMRE	Tetramethylrhodamine ethyl ester
TNF	Tumor Necrosis Factor
TPM	Transcripts Per Million
TU/mL	Transduction units per milliliter
γH2AX	gamma (phosphorylated) histone H2AX (Ser139)

Supplementary Information

The online version contains supplementary material available at https://doi.org/10.1186/s12943-025-02542-0.

Supplementary Material 1.

Acknowledgements

We would like to express our gratitude to Juan Bueren and Paula Río from the Division of Hematopoietic Innovative Therapies, Biomedical Innovation Unit, Centro de Investigaciones Energéticas, Medioambientales y Tecnológicas (CIEMAT) for their invaluable support and dedication in reviewing and improving this manuscript. Their insightful feedback and contributions have been instrumental in refining our work. We thank the Microarrays Unit at the Josep Carreras Leukemia Research Institute for assistance with OGM, in particular Mar Mallo and Kiko Solé, and we are also grateful to Alicia Barroso, Miguel Angel Grillo y Eduardo Gil (CNIO) for their support with GUIDE-seq library preparation.

Authors' contributions

A.N-S., M.M-L., P.P-S., A.A-Y., P.O-W., F.J.M., C.M., M.C.M., S.C. M.I-N., L.F., G.P., R.A., R.N-T. and R.T-R. performed experimental investigation. A.N-S., M.M-L., P.P-S, A.G-N. and LA-G conducted data analysis. A.N-S., M.M-L., R.T-R. and S.R-P. prepared figures. A.N-S. and S.R-P. wrote the manuscript. V.J.S-A.L., N.M. and P.R-N. reviewed and edited the manuscript. R.T-R. and S.R-P. coordinated and conceptualize the project.

Funding

This work was supported by grants from the Spanish National Research and Development Plan, Instituto de Salud Carlos III, and FEDER (PI20/01837 and PI23/01932 to S.R-P. and PI21/01641 to R.T-R); and AECC (AECC_Lab 2020) to S.R-P. Additionally, V.J.S-A.L. received funding from the Ayudas a la Investigación UFV Grant [grant number UFV2022-23] and ISCIII/FEDER [grant number PI22/00492], and P.R-N. from PID2020-115444GB-I00 (MCIN/AEI/https://doi.org/10.13039/501100011033). A.N. is supported by a PhD fellowship from the Comunidad Autonoma de Madrid, P.P-S. is supported by a FPU PhD fellowship and A.A-Y is supported by a La Caixa PhD fellowship. P.O-W. is supported by the European Union's Horizon Europe programme under grant agreement No. 101070950 (X-PAND).

Data availability

The raw data generated in this study are available from the corresponding author upon reasonable request. The NGS/OGM data have been deposited in the BioProject database under the accession code PRJNA1357324.

Declarations

Ethics approval and consent to participate

All experiments with mice conformed to Animal Welfare guidelines and were performed in accordance to protocols approved by the Ethics Committee of the Instituto de Salud Carlos III (No. IACUC.001-2021).

Consent for publication

Not applicable.

Competing interests

The authors declare no competing interests.

Author details

[1]Molecular Cytogenetics and Genome Editing Unit, Human Cancer Genetics Programme, Spanish National Cancer Centre (CNIO), Madrid, Spain
[2]Division of Hematopoietic Innovative Therapies, Biomedical Innovation Unit, Centro de Investigaciones Energéticas, Medioambientales y Tecnológicas (Ciemat), Madrid, Spain
[3]Advanced Therapies Unit, Instituto de Investigación Sanitaria Fundación Jiménez Díaz, Madrid, Spain
[4]Centro de Investigación Biomédica en Red de Enfermedades Raras, Madrid, Spain

[5]Pediatric Onco-Hematology Clinical Reseacrh Unit IdiPAZ-CNIO, Madrid, Spain
[6]Human Genotyping Unit-CEGEN, Human Cancer Genetics Programme, Spanish National Cancer Centre (CNIO), Madrid, Spain
[7]Grupo de Oncología Molecular, Instituto de Investigaciones Biosanitarias, Facultad de Ciencias Experimentales, Universidad Francisco de Vitoria (UFV), Madrid, Spain
[8]Grupo de Oncología Cutánea. Servicio de Anatomía Patológica, Hospital Universitario 12 de Octubre. Instituto de Investigación Sanitaria Hospital 12 de Octubre (imas12), Madrid, Spain
[9]Genetic and Molecular Epidemiology group, Human Cancer Genetics Programme, Spanish National Cancer Centre (CNIO), and CIBERONC, Madrid, Spain
[10]Department of Immunology, Ophthalmology and ENT, School of Medicine, Universidad Complutense de Madrid, 12 de Octubre Health Research Institute (imas12), Madrid, Spain

Received: 18 July 2025 / Accepted: 1 December 2025
Published online: 22 December 2025

References

1. Pons G, Gallo-Oller G, Navarro N, Zarzosa P, Sansa-Girona J, Garcia-Gilabert L, Magdaleno A, Segura MF, de Sanchez J, Gallego S, et al. Analysis of cancer genomic amplifications identifies druggable collateral dependencies within the amplicon. Cancers (Basel). 2023;15(6). https://doi.org/10.3390/cancers15061636.
2. Shoshani O, Brunner SF, Yaeger R, Ly P, Nechemia-Arbely Y, Kim DH, Fang R, Castillon GA, Yu M, Li JSZ, et al. Chromothripsis drives the evolution of gene amplification in cancer. Nature. 2021;591(7848):137–41.
3. Verhaak RGW, Bafna V, Mischel PS. Extrachromosomal oncogene amplification in tumour pathogenesis and evolution. Nat Rev Cancer. 2019;19(5):283–8.
4. Kadali VN, Shoshani O. Aberrant nuclei with amplified DNA in cancer. Trends Cancer. 2025;11(1):9–11.
5. Yang QL, Xie Y, Qiao K, Lim JYS, Wu S. Modern biology of extrachromosomal DNA: a decade-long voyage of discovery. Cell Res. 2025;35(1):11–22.
6. Raeisi Dehkordi S, Wong IT, Ni J, Luebeck J, Zhu K, Prasad G, Krockenberger L, Xu G, Chowdhury B, Rajkumar U, et al. Breakage fusion Bridge cycles drive high oncogene number with moderate intratumoural heterogeneity. Nat Commun. 2025;16(1):1497.
7. Storlazzi CT, Lonoce A, Guastadisegni MC, Trombetta D, D'Addabbo P, Daniele G, L'Abbate A, Macchia G, Surace C, Kok K, et al. Gene amplification as double minutes or homogeneously staining regions in solid tumors: origin and structure. Genome Res. 2010;20(9):1198–206.
8. Turner KM, Deshpande V, Beyter D, Koga T, Rusert J, Lee C, Li B, Arden K, Ren B, Nathanson DA, et al. Extrachromosomal oncogene amplification drives tumour evolution and genetic heterogeneity. Nature. 2017;543(7643):122–5.
9. Kim H, Nguyen NP, Turner K, Wu S, Gujar AD, Luebeck J, Liu J, Deshpande V, Rajkumar U, Namburi S, et al. Extrachromosomal DNA is associated with oncogene amplification and poor outcome across multiple cancers. Nat Genet. 2020;52(9):891–7.
10. Hung KL, Yost KE, Xie L, Shi Q, Helmsauer K, Luebeck J, Schopflin R, Lange JT, Chamorro Gonzalez R, Weiser NE, et al. EcDNA hubs drive cooperative intermolecular oncogene expression. Nature. 2021;600(7890):731–6.
11. Yang L, Jia R, Ge T, Ge S, Zhuang A, Chai P, Fan X. Extrachromosomal circular DNA: biogenesis, structure, functions and diseases. Signal Transduct Target Ther. 2022;7(1):342.
12. Hung KL, Jones MG, Wong IT, Curtis EJ, Lange JT, He BJ, Luebeck J, Schmargon R, Scanu E, Bruckner L, et al. Coordinated inheritance of extrachromosomal DNAs in cancer cells. Nature. 2024;635(8037):201–9.
13. Lange JT, Rose JC, Chen CY, Pichugin Y, Xie L, Tang J, Hung KL, Yost KE, Shi Q, Erb ML, et al. The evolutionary dynamics of extrachromosomal DNA in human cancers. Nat Genet. 2022;54(10):1527–33.
14. Nathanson DA, Gini B, Mottahedeh J, Visnyei K, Koga T, Gomez G, Eskin A, Hwang K, Wang J, Masui K, et al. Targeted therapy resistance mediated by dynamic regulation of extrachromosomal mutant EGFR DNA. Science. 2014;343(6166):72–6.
15. Ramos Elbal E, Galera Minarro AM, Llinares Riestra ME, Bermudez Cortes M, Fuster Soler JL. Neuroblastoma: validation of the INRG classification system in a small series. Clin Transl Oncol. 2019;21(12):1776–80.
16. Smith V, Foster J. High-Risk neuroblastoma treatment review. Child (Basel). 2018;5(9). https://doi.org/10.3390/children5090114.
17. Whittle SB, Smith V, Doherty E, Zhao S, McCarty S, Zage PE. Overview and recent advances in the treatment of neuroblastoma. Expert Rev Anticancer Ther. 2017;17(4):369–86.
18. Lee JW, Son MH, Cho HW, Ma YE, Yoo KH, Sung KW, Koo HH. Clinical significance of MYCN amplification in patients with high-risk neuroblastoma. Pediatr Blood Cancer. 2018;65(10):e27257.
19. Otte J, Dyberg C, Pepich A, Johnsen JI. MYCN function in neuroblastoma development. Front Oncol. 2020;10:624079.
20. Kwak Y, Yun S, Nam SK, Seo AN, Lee KS, Shin E, Oh HK, Kim DW, Kang SB, Kim WH, et al. Comparative analysis of the EGFR, HER2, c-MYC, and MET variations in colorectal cancer determined by three different measures: gene copy number gain, amplification status and the 2013 ASCO/CAP guideline criterion for HER2 testing of breast cancer. J Transl Med. 2017;15(1):167.
21. Mollaoglu G, Guthrie MR, Bohm S, Bragelmann J, Can I, Ballieu PM, Marx A, George J, Heinen C, Chalishazar MD, et al. MYC drives progression of small cell lung cancer to a variant neuroendocrine subtype with vulnerability to Aurora kinase Inhibition. Cancer Cell. 2017;31(2):270–85.
22. Zimmerli D, Brambillasca CS, Talens F, Bhin J, Linstra R, Romanens L, et al. MYC promotes immune-suppression in triple-negative breast cancer via inhibition of interferon signaling. Nat Commun. 2022;13(1):6579.
23. Li J, Dong T, Wu Z, Zhu D, Gu H. The effects of MYC on tumor immunity and immunotherapy. Cell Death Discov. 2023;9(1):103.
24. Tang J, Weiser NE, Wang G, Chowdhry S, Curtis EJ, Zhao Y, Wong IT, Marinov GK, Li R, Hanoian P, et al. Enhancing transcription-replication conflict targets ecDNA-positive cancers. Nature. 2024;635(8037):210–8.
25. Bei Y, Brame L, Kirchner M, Fritsche-Guenther R, Kunz S, Bhattacharya A, Rusu MC, Gurgen D, Dubios FPB, Koppke JKC, et al. Passenger gene coamplifications create collateral therapeutic vulnerabilities in cancer. Cancer Discov. 2024;14(3):492–507.
26. Kwon T, Ra JS, Lee S, Baek IJ, Khim KW, Lee EA, Song EK, Otarbayev D, Jung W, Park YH et al. Precision targeting tumor cells using cancer-specific InDel mutations with CRISPR-Cas9. Proc Natl Acad Sci U S A. 2022;119(9). https://doi.org/10.1073/pnas.2103532119}
27. Hanlon MB, Shohet JM, Wolfe SA. Selective targeting of genome amplifications and repeat elements by CRISPR-Cas9 nickases to promote cancer cell death. Nat Commun. 2025;16(1):5126.
28. Kroemer G, Galassi C, Zitvogel L, Galluzzi L. Immunogenic cell stress and death. Nat Immunol. 2022;23(4):487–500.
29. Shen R, Liu D, Wang X, Guo Z, Sun H, Song Y, Wang D. DNA damage and activation of cGAS/STING pathway induce tumor microenvironment remodeling. Front Cell Dev Biol. 2021;9:828657.
30. Dey P, Kimmelman AC, DePinho RA. Metabolic codependencies in the tumor microenvironment. Cancer Discov. 2021;11(5):1067–81.
31. da Costa A, Chowdhury D, Shapiro GI, D'Andrea AD, Konstantinopoulos PA. Targeting replication stress in cancer therapy. Nat Rev Drug Discov. 2023;22(1):38–58.
32. Hopkins JL, Lan L, Zou L. DNA repair defects in cancer and therapeutic opportunities. Genes Dev. 2022;36(5–6):278–93.
33. Martinez-Lage M, Torres-Ruiz R, Puig-Serra P, Moreno-Gaona P, Martin MC, Moya FJ, Quintana-Bustamante O, Garcia-Silva S, Carcaboso AM, Petazzi P, et al. In vivo CRISPR/Cas9 targeting of fusion oncogenes for selective elimination of cancer cells. Nat Commun. 2020;11(1):5060.
34. Tan IL, Perez AR, Lew RJ, Sun X, Baldwin A, Zhu YK, Shah MM, Berger MS, Doudna JA, Fellmann C. Targeting the non-coding genome and Temozolomide signature enables CRISPR-mediated glioma Oncolysis. Cell Rep. 2023;42(11):113339.
35. de Visser KE, Joyce JA. The evolving tumor microenvironment: from cancer initiation to metastatic outgrowth. Cancer Cell. 2023;41(3):374–403.
36. Bao R, Spranger S, Hernandez K, Zha Y, Pytel P, Luke JJ, Gajewski TF, Volchenboum SL, Cohn SL, Desai AV. Immunogenomic determinants of tumor microenvironment correlate with superior survival in high-risk neuroblastoma. J Immunother Cancer. 2021;9(7). https://doi.org/10.1136/jitc-2021-002417.
37. Rivera Z, Escutia C, Madonna MB, Gupta KH. Biological insight and recent advancement in the treatment of neuroblastoma. Int J Mol Sci. 2023;24(10). https://doi.org/10.1136/ijms24108470.
38. Seier JA, Reinhardt J, Saraf K, Ng SS, Layer JP, Corvino D, Althoff K, Giordano FA, Schramm A, Fischer M, et al. Druggable epigenetic suppression of interferon-induced chemokine expression linked to MYCN amplification in neuroblastoma. J Immunother Cancer. 2021;9(5). https://doi.org/10.1136/jitc-2020-001335.

39. Bailey C, Pich O, Thol K, Watkins TBK, Luebeck J, Rowan A, Stavrou G, Weiser NE, Dameracharla B, Bentham R, et al. Origins and impact of extrachromosomal DNA. Nature. 2024;635(8037):193–200.
40. Henssen A, Althoff K, Odersky A, Beckers A, Koche R, Speleman F, Schafers S, Bell E, Nortmeyer M, Westermann F, et al. Targeting MYCN-Driven transcription by BET-Bromodomain Inhibition. Clin Cancer Res. 2016;22(10):2470–81.
41. Shiraishi D, Fujiwara Y, Horlad H, Saito Y, Iriki T, Tsuboki J, Cheng P, Nakagata N, Mizuta H, Bekki H, et al. CD163 is required for protumoral activation of macrophages in human and murine sarcoma. Cancer Res. 2018;78(12):3255–66.
42. Stip MC, Teeuwen L, Dierselhuis MP, Leusen JHW, Krijgsman D. Targeting the myeloid microenvironment in neuroblastoma. J Exp Clin Cancer Res. 2023;42(1):337.
43. Wu X, Nelson M, Basu M, Srinivasan P, Lazarski C, Zhang P, Zheng P, Sandler AD. MYC oncogene is associated with suppression of tumor immunity and targeting Myc induces tumor cell immunogenicity for therapeutic whole cell vaccination. J Immunother Cancer. 2021;9(3). https://doi.org/10.1136/jitc-2020-001388.
44. Kim YH, Kim N, Okafor I, Choi S, Min S, Lee J, Bae SM, Choi K, Choi J, Harihar V, et al. Sniper2L is a high-fidelity Cas9 variant with high activity. Nat Chem Biol. 2023;19(8):972–80.
45. Zhang H, Kelly K, Lee J, Echeverria D, Cooper D, Panwala R, Amrani N, Chen Z, Gaston N, Wagh A, et al. Self-delivering, chemically modified CRISPR RNAs for AAV co-delivery and genome editing in vivo. Nucleic Acids Res. 2024;52(2):977–97.
46. Radmand A, Kim H, Beyersdorf J, Dobrowolski CN, Zenhausern R, Paunovska K, Huayamares SG, Hua X, Han K, Loughrey D, et al. Cationic cholesterol-dependent LNP delivery to lung stem cells, the liver, and heart. Proc Natl Acad Sci U S A. 2024;121(11):e2307801120.
47. Ling S, Zhang X, Dai Y, Jiang Z, Zhou X, Lu S, et al. Customizable virus-like particles deliver CRISPR-Cas9 ribonucleoprotein for effective ocular neovascular and Huntington's disease gene therapy. Nat Nanotechnol. 2025;20(4):543–53.
48. Dou L, Fang Y, Yang H, Ai G, Shen N. Immunogenic cell death: A new strategy to enhancing cancer immunotherapy. Hum Vaccin Immunother. 2024;20(1):2437918.
49. Zhou Z, Mai Y, Zhang G, Wang Y, Sun P, Jing Z, Li Z, Xu Y, Han B, Liu J. Emerging role of Immunogenic cell death in cancer immunotherapy: advancing next-generation CAR-T cell immunotherapy by combination. Cancer Lett. 2024;598:217079.
50. Rodriguez-Perales S, Torres-Ruiz R, Suela J, Acquadro F, Martin MC, Yebra E, Ramirez JC, Alvarez S, Cigudosa JC. Truncated RUNX1 protein generated by a novel t(1;21)(p32;q22) chromosomal translocation impairs the proliferation and differentiation of human hematopoietic progenitors. Oncogene. 2016;35(1):125–34.
51. Konda P, Roque Iii JA, Lifshits LM, Alcos A, Azzam E, Shi G, Cameron CG, McFarland SA, Gujar S. Photodynamic therapy of melanoma with new, structurally similar, NIR-absorbing ruthenium (II) complexes promotes tumor growth control via distinct hallmarks of Immunogenic cell death. Am J Cancer Res. 2022;12(1):210–28.
52. Malinin NL, Lee G, Lazzarotto CR, Li Y, Zheng Z, Nguyen NT, Liebers M, Topkar VV, Iafrate AJ, Le LP, et al. Defining genome-wide CRISPR-Cas genome-editing nuclease activity with GUIDE-seq. Nat Protoc. 2021;16(12):5592–615.
53. Tsai SQ, Topkar VV, Joung JK, Aryee MJ. Open-source Guideseq software for analysis of GUIDE-seq data. Nat Biotechnol. 2016;34(5):483.

Publisher's Note